## ADVANCES IN CHARACTERIZATION OF DEFORMATION STRUCTURES BY HIGH RESOLUTION RECIPROCAL SPACE MAPPING

W. Pantleon*,
C. Wejdemann*, B. Jakobsen*,**, U. Lienert***, and H.F. Poulsen*

* Center for Fundamental Research: Metal Structures in Four
Dimensions, Materials Research Division, Risø National
Laboratory for Sustainable Energy, Technical University of
Denmark, Frederiksborgvej 399, 4000 Roskilde, Denmark
** Center of Fundamental Research: Glass and Time, Department
of Science, Systems and Models, Roskilde University,
Universitetsvej 1, 4000 Roskilde, Denmark
*** Advanced Photon Source, Argonne National Laboratory, 9700
South Cass Avenue, Argonne, IL 60439, USA

## ABSTRACT

With high angular resolution three-dimensional X-ray diffraction quantitative information is gained about dislocation structures in individual grains in the bulk of a macroscopic specimen by acquiring reciprocal space maps. In high resolution three-dimensional reciprocal space maps of tensile deformed copper, individual, almost dislocation-free subgrains are identified from high-intensity peaks and distinguished by their unique combination of orientation and elastic strain; dislocation walls manifest themselves as a smooth cloud of lower intensity. The elastic strains show only minor variations within each subgrain, but larger variations between different subgrains. In average, subgrains experience back strains, whereas dislocations walls are strained in forward direction. Based on these observations a revision of the classical composite model is formulated. Additionally, subgrain dynamics is followed *in-situ* during varying loading conditions by reciprocal space mapping: During uninterrupted tensile deformation, formation of subgrains can be observed concurrently with broadening of Bragg reflections shortly after onset of plastic deformation. The emergence of dislocation-free regions proofs that ordered dislocation structures develop during tensile deformation. With continued tensile deformation, the subgrain structure develops intermittently. When the traction is terminated, stress relaxation occurs and no changes in the number, size and orientation of the subgrains are observed. When changing the tensile direction after pre-deformation in tension, a systematic correlation between the degree of strain path change and the volume fraction of the subgrains is established. In case of perpendicular tensile axes, a reversal of the radial profile asymmetry is observed and explained.

## 1. INTRODUCTION

During plastic deformation of metals, dislocations are stored in the material. In pure face centered cubic metals, such as aluminium and copper, they organize into heterogeneous dislocation structures characteristic of the material and the deformation conditions. As the formed dislocation structure influences the mechanical properties of the metal, understanding of the origin and evolution of ordered dislocation structures is relevant for predicting their flow stresses and work-hardening rates (e.g. Gil Sevillano 1993).

The dislocation structures formed during deformation of copper have been studied extensively (e.g. Essmann 1963; Steeds 1966; Göttler 1973; Knoesen and Kritzinger 1982; Huang 1998). Dislocations organize in ordered structures consisting of almost dislocation-free regions (subgrains) separated by dislocations walls of high dislocation density; the scale of the structure decreases inversely with increasing flow stress (Raj and Pharr 1986). The specific morphology depends on the deformation conditions and the orientation of the crystalline lattice (Huang 1998). Changes in the deformation conditions require the dislocation structure to reorganize and adapt to the new deformation conditions, after e.g. strain path changes (Schmitt, Fernandes, Gracio, and Vieira 1991; Sakharova and Fernandes 2006).

The processes involved in dislocation structure formation, evolution and adaptation to the applied loading conditions are still not well understood, partly because no experimental techniques have been available to study the dynamics involved. The experiment described in this paper aims to further the understanding of these phenomena by studying the evolution of dislocation structures *in-situ* during a variety of loading conditions.

Traditionally dislocation structures are studied with either classical X-ray line profile analysis (Wilkens 1970a; Krivoglaz 1996; Breuer, Klimanek, and Pantleon 2000; Ungár 2001; Kužel 2007) or transmission electron microscopy (Essmann 1963; Steeds 1966; Göttler 1973; Knoesen and Kritzinger 1982; Huang 1998). TEM is able to produce high resolution images of the dislocation structures in direct space, but has the disadvantage that bulk grains cannot be studied *in-situ* because macroscopic samples must be destroyed to produce the thin foils necessary for electron transmission. Furthermore, investigating the evolution of dislocation structures *in-situ* in thin foils is not representative for the behavior in the bulk due to image forces from the free surfaces. Conventional X-ray line profile analysis has the disadvantage of averaging over many grains as the measured diffraction signal originates from different grains with even different orientations.

Over the last decade, two synchrotron radiation based techniques for three-dimensional characterization have been established. The spatial resolution of the 3D X-Ray Diffraction (3DXRD) microscope (Poulsen, Nielsen, Lauridsen, Schmidt, Suter, Lienert, Margulies, Lorentzen, and Juul Jensen 2001) enables investigating individual grains in the bulk of a specimen, but its limited spatial and angular resolution does not allow for direct observation of deformation structures with their small orientation differences on a scale of about a micrometer. The spatial scanning technique of the 3D X-ray crystal microscope (Larson, Yang, Ice, Budai, and Tischler 2002) limits the possibility of investigating the dynamics of structural changes and is more suitable for near-surface investigations.

By supplementing 3DXRD with high angular resolution (Jakobsen, Poulsen, Lienert, Almer, Shastri, Sørensen, Gundlach, and Pantleon 2006) dislocation structures can be studied by obtaining high resolution three-dimensional reciprocal space maps of Bragg reflections from individual bulk grains *in-situ* during loading. The opportunities of the method are illustrated for loading differently pre-conditioned copper samples in tension.

## 2. EXPERIMENTAL TECHNIQUE

2.1 Setup. At beamline 1-ID-XOR at the Advanced Photon Source (APS, Argonne National Laboratory) a special setup for obtaining three-dimensional reciprocal space maps of individual bulk grains with high resolution is established (Jakobsen et al. 2006). An X-ray energy of 52 keV gives a penetration depth of about 500 $\mu$m in copper, and makes it possible to obtain diffraction patterns from bulk grains. A narrow beam with a height of 25 $\mu$m and a width of 30 $\mu$m ensures that only a small volume of the sample is illuminated, which is necessary for studying selected individual grains in order to avoid overlap with reflections from other grains. The narrow beam is conditioned by vertical focusing (giving a vertical divergence of 17 $\mu$rad) and horizontal slits. Focusing increases the flux and thereby reduces the acquisition time. High angular resolution is achieved by combining a narrow-bandwidth monochromator ($\Delta E/E = 7 \cdot 10^{-5}$) and a large sample-detector distance (3.6 m). A two-dimensional detector with a pixel size of 80 $\mu$m is mounted above the beam and centered at a height of a 400 reflection (for copper) as shown in Figure 1. A two-dimensional image (as illustrated in Figure 2) is acquired while rocking (rotating with constant angular velocity) the sample through a small angle interval around the horizontal axis perpendicular to the scattering plane (the $\omega$-axis in Figure 1).
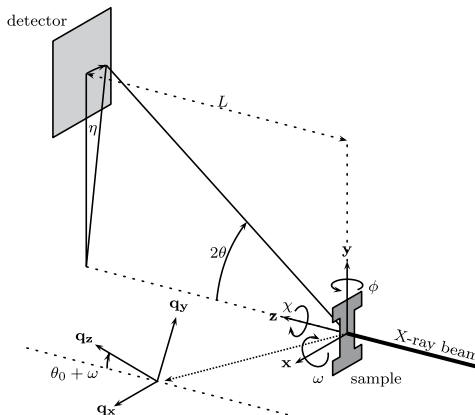


Fig. 1: Sketch of setup with far distant detector (from Jakobsen et al. 2007a).

By combining several images a three-dimensional reciprocal space map is obtained where two dimensions are given by the horizontal and vertical directions on the detector and the third dimension arises from subsequent rocking intervals. The resolution of the method is $1 \cdot 10^{-3}$ Å$^{-1}$ in the two detector directions (determined by detector pixel size, beam divergence and beam energy spread) and similar in the third direction (determined by the chosen rocking angle interval, $1 \cdot 10^{-3}$ Å$^{-1}$ for 0.007° or $2 \cdot 10^{-3}$ Å$^{-1}$ for 0.015°). A detailed description of the setup can be found in (Jakobsen, Poulsen, Lienert, and Pantleon 2007a).

2.2 Specimen. The sample material is 99.99% pure oxygen-free high conductivity (OFHC) polycrystalline copper initially cold-rolled and fully recrystallized by annealing for 120 min at 450 °C. Subsequent characterization by electron backscatter diffraction reveals that the sheets are fully recrystallized with a mean chord length (ignoring twin boundaries) between 20 to 30 $\mu$m and that their texture is weak. Dog-bone shaped tensile samples with a gauge length of 8 mm and a gauge width of 3 mm are prepared from the 300 $\mu$m thick sheets by spark cutting. All investigations reported here are performed at room temperature.

2.3 Experimental procedure. For *in-situ* deformation, tensile samples are mounted in a custom-made load frame with a strain gauge glued onto the gauge area. For each sample a suitable grain is selected, and one particular 400 reflection is mapped at different strain levels as the sample is deformed in tension. A large area two-dimensional detector near the sample (and centered with respect to the primary beam) is used for finding suitable grains which fulfill four criteria (Wejdemann, Poulsen, Lienert and Pantleon 2009): 1) The [400] direction must be nearly parallel to the tensile axis. 2) The chosen 400 reflection must be well separated from reflections from other grains. 3) The grain must be completely illuminated by the beam which requires that the grain size of the selected grain is smaller than the beam size. The grain size is estimated by scanning the grain through the beam and measuring the diffracted intensity as function of position. 4) The grain must be in the bulk of the specimen and must not be near the surface. The position of the grain with respect to the sample surface is determined by a simple geometric method (Wejdemann, Lienert, Nielsen and Pantleon 2010b). Some grains are excluded because the scan through the beam shows a profile with two distinct intensity maxima indicating the presence of a twin lamella in the grain, others are excluded because their orientation spread is too large which would make the time required for a full mapping too long.

After a suitable grain is selected, the near detector is moved out of the X-ray path. By means of an Eulerian cradle, the sample is oriented so that the 400 reflection from the grain is observed on the far detector. With this detector two-dimensional images of the 400 reflection are obtained while rocking the sample around the $\omega$-axis perpendicular to the main scattering plane. When the rocking interval is large enough to cover the entire orientation spread of the grain, smooth intensity distributions are recorded. For smaller rocking intervals, however, a more detailed structure of the Bragg reflection is revealed and the detector images show characteristic features related to the dislocation structure in the grain. As shown for a detector image obtained by rocking over an interval of 0.007° in Figure 2, the images contain localized areas with high-intensity peaks superimposed on a slowly varying cloud of lower intensity (still enhanced compared to the background). This characteristic feature is observed for all reflections from grains in tensile deformed copper. As discussed later, the high-intensity peaks are produced by almost dislocation-free regions of the crystal (subgrains) while the spread-out cloud is caused by regions with a high dislocation density (dislocation walls) (Jakobsen et al. 2006, 2007a, 2008).

2.4 Data presentation. Three-dimensional reciprocal space maps are gathered by combining a number of two-dimensional detector images (such as shown in Figure 2), each acquired by exposing the sample while rocking it through a small interval around the $\omega$-axis. The information in such three-dimensional intensity distributions can be conveniently presented in two complementary projections: (i) radial peak profiles and (ii) projections of the intensity distribution onto the azimuthal plane.

Radial peak profiles are obtained by integrating over the directions perpendicular to the diffraction vector (the azimuthal directions). They characterize the intensity distribution along the scattering vector

$$q_y = \frac{4\pi}{\lambda} \sin(\vartheta) \,. \tag{1}$$

Shifts $\Delta q_y$ in the radial component are related to shifts $\Delta\vartheta = \vartheta - \vartheta_0$ in the diffraction angle $\vartheta$ from the undisturbed Bragg angle $\vartheta_0$ and indicate the presence of elastic lattice strains

$$\varepsilon = -\frac{\Delta q_y}{q_y} = -\Delta\vartheta \, \cot\vartheta_0 \,. \tag{2}$$

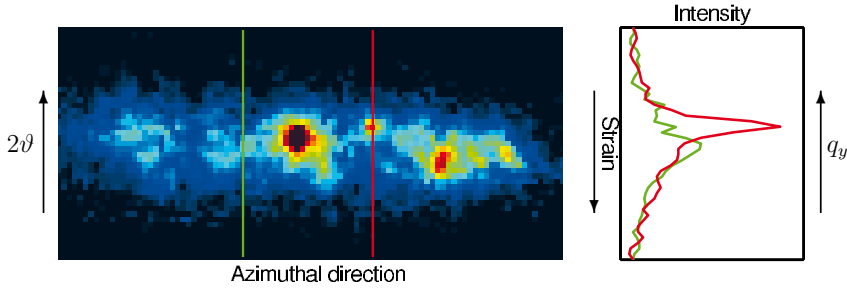Fig. 2: Detector image (left) of a 400 reflection close to the tensile axis after 2% tensile strain obtained by rocking over an interval of 0.007° with radial direction vertically and an azimuthal direction horizontally. From the intensity distribution sharp peaks are clearly visible on top of a cloud of lower intensity. The right part shows two cuts through the intensity distribution along the radial direction (along the lines of same colour in the left panel). From the different radial position of the maxima of these radial profiles, strain differences between cloud and peak are obvious.

An example for an integrated radial profile is presented by the black line in Figure 3. The radial profile is broadened and asymmetric. The broadening is mainly caused by heterogeneous microstrains in the grain as any contribution from size broadening or twinning can be neglected (due to the large grain size above a micrometer and the low twinning probability).
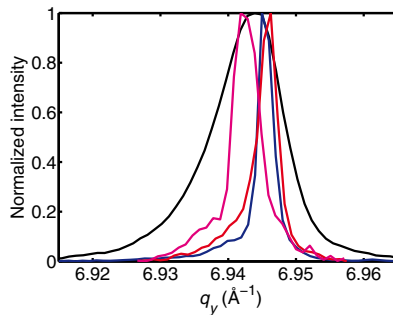


Fig. 3: Radial profile (black) from a 400 reflection integrated over an entire grain after 3.49% tensile strain. Radial profiles of three selected subgrains in red, blue and magenta (from Jakobsen et al. 2006).

A representation of the orientation spread can be gained from projections of the intensity distribution onto the plane perpendicular to the diffraction vector, i.e. spanned by the horizontal detector direction and the rocking direction. Such an azimuthal projection is obtained by integrating the intensity distribution over the radial component of the diffraction vector. It represents the 400 pole figure (the distribution of normal vectors of the crystallographic (400) lattice planes) of the selected grain and visualizes the mosaic spread within the grain. An example for an azimuthal projection of a 400 reflection after 2% tensile strain is shown in Figure 4. With the colour scale used, the map comprises separate individual high-intensity peaks, large islands and a rather smooth low-intensity cloud. As seen in the insert, the island is also composed of high-intensity peaks, some of them so close to each other that they partially overlap.
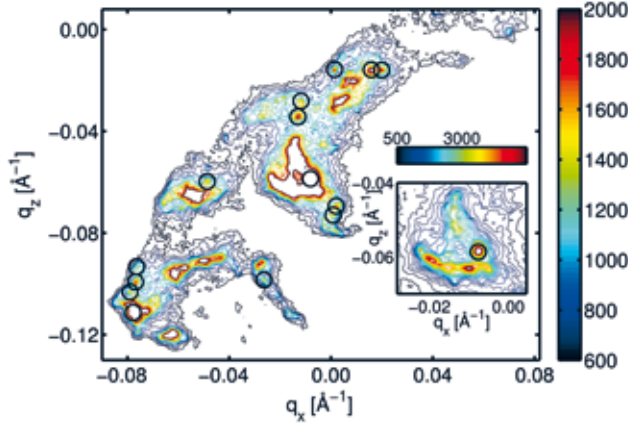
Fig. 4: 400 reflection of a grain after 2% tensile strain: Projection of the three-dimensional intensity distribution in reciprocal space on the azimuthal plane. Circles indicate the azimuthal positions of 14 selected peaks (from Jakobsen et al. 2007a).

2.5 High-intensity peaks and subgrains. Comprehensive information on an independently diffracting region can be gained from each distinct peak. A detailed analysis of 14 high-intensity peaks (marked by circles in Figure 4) is performed after 2% tensile strain (Jakobsen et al. 2007a): pseudo-Voigt functions are fitted to the intensity distribution of each individual peak along the three directions of reciprocal space. In this manner, the volume of the individual diffracting regions is derived from the integrated intensity of the high-intensity peaks, while their mean orientation and their mean elastic strain (along the scattering vector) are determined by the center-of-mass position in azimuthal and radial directions, respectively. From the peak shape, orientation and elastic strain differences as well as the dislocation density within the individually diffracting regions are inferred.

The volumes of the different regions giving rise to the individual peaks are between 1 and 5 $\mu$m$^3$. The widths of the individual sharp peaks in all three dimensions of reciprocal space are similar, rather small ($\langle \Delta q \rangle = 1.9 \cdot 10^{-3}$ Å$^{-1}$), and comparable to an undeformed grain suggesting their interpretation as originating from dislocation-free subgrains.

The radial profile integrated over the entire orientation spread of the grain (shown in Figure 5(left)) is broadened with a full width at half of maximum intensity of $6.4 \cdot 10^{-3}$ Å$^{-1}$ and asymmetric with a longer tail at smaller radial components $q_y$. The radial profiles of individual high-intensity peaks are much sharper ($\langle \Delta q_y \rangle = 2 \cdot 10^{-3}$Å$^{-1}$) indicating small intrasubgrain strains (below 0.03%) and a rather low dislocation density (compare Figure 3 for a similar observation at 3.49% tensile strain).

For a quantitative assessment of the dislocation density, the measured width must be corrected for instrumental broadening and possible size effects. An upper limit $\langle \Delta q_{y,corr} \rangle = 1.7 \cdot 10^{-3}$Å$^{-1}$ for the physical width results by using a lower limit for the instrumental resolution. Estimation of the dislocation densities by the theory of Wilkens (1970a; 1970b) shows that the dislocation density cannot exceed $1.2 \cdot 10^{13}$ m$^{-2}$ in such a nearly dislocation-free region (Jakobsen et al. 2007a). The dislocation density really present in the subgrain is, however, expected to be much less, because the estimate for the physical width is derived under the most optimistic assumptions and constitutes an upper limit.
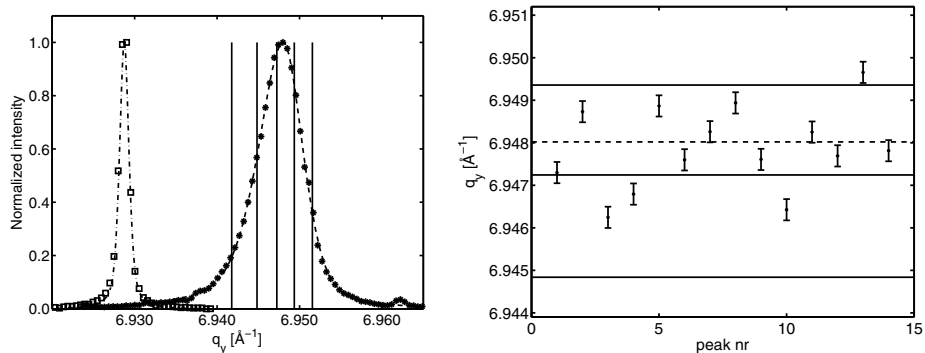
Fig. 5: (left) Radial profile for the entire grain after 2% tensile strain (dots) and $LaB_6$ powder (open squares) for comparison. Vertical solid lines indicate the 10%, 25%, 50% 75% and 90% quantiles. The dashed lines are fits of a split pseudo-Voigt and a pseudo-Voigt function to the measured profiles of Cu and $LaB_6$, respectively.
(right) Radial peak position for 14 isolated peaks. The dashed horizontal line indicates the position of the maximum of the radial profile of the integrated reflection from the entire grain and the full lines the 25%, 50% and 75% quantiles of that profile. The average radial position for the entire grain (6.9473 $\mathring{A}^{-1}$) is close to the median (50% quantile) of the profile (from Jakobsen et al. 2007a).

In contrast to the small intrasubgrain stresses, significant intersubgrain stresses exist as obvious from Figure 5(right). The radial peak positions of the subgrains are not gathered around the median or average value of the radial profile, but concentrate around the position of maximum intensity of the integrated profile. The difference between individual radial peak positions is up to $3.5 \cdot 10^{-3} \mathring{A}^{-1}$ corresponding to a difference of 0.05% in elastic strain (or a stress difference of 33 MPa). In average the subgrains experience an elastic back strain of 0.009% (corresponding to a back stress of 6 MPa) with respect to the average tensile elastic strain of the entire grain.

2.6 Cloud contribution. Additional to integrated radial profiles (which can also be obtained by conventional X-ray diffraction) radial profiles at each particular azimuthal position can be determined from the three-dimensional reciprocal space maps. Two such radial profiles are illustrated on the right of Figure 2. In case a high-intensity peak is hit, the profile becomes rather sharp and has a high maximal intensity, whereas in the other case a smooth broadened profile with low maximum intensity is detected. Notably, the radial positions of both maxima are different. The maximum of the sharp profile occurs at higher $q_y$ indicative for a negative elastic strain compared to the maximum of the broad profile.

This effect is analyzed in more detail for another grain after 2% deformation (Jakobsen, Lienert, Almer, Poulsen, and Pantleon 2008) by comparing radial profiles along each available azimuthal position. For each of these radial profiles the maximum intensity $I_{max}$ and its radial position $q_{y,max}$ is determined and the average radial position is calculated for all profiles with similar maximal intensity. The resulting Figure 6 shows a strong correlation between the maximal intensity and the radial positions of the maxima (converted to elastic strain with respect to the grain average by Eq. (2)). Low-intensity maxima are positioned at more positive strains (lower $q_y$) than maxima of higher intensity. Comparison with the maximum and average position of the integrated peak profile reveals that the maxima of

highest intensity fall close to the maximum of the integrated radial peak profile and that for the maxima with very low intensity the averages are at radial positions below the average of the integrated radial peak profile corresponding to forward elastic strains. Regions giving rise to the cloud of low intensity have forward strains, whereas the regions giving rise to the high-intensity peaks have negative elastic strain (backward strains).
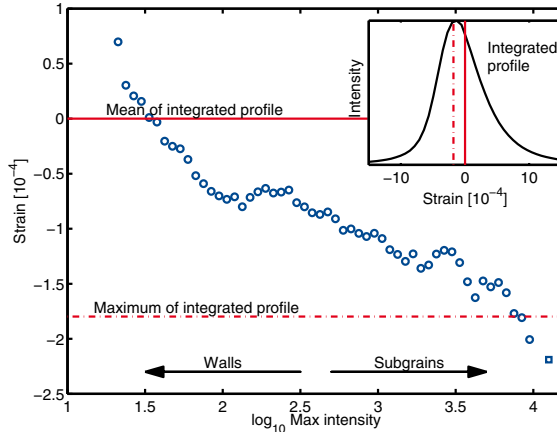


Fig. 6: Average strain at maximum intensity in dependence on the maximum intensity along radial profiles. High-intensity regions have negative elastic strains (with respect to the average elastic strain of the entire grain after 2% tension) and low-intensity regions positive strains. The insert shows the asymmetric integrated radial profile for the entire grain (see Jakobsen et al. 2008).

## 3. INTERPRETATION

3.1 Classical composite model. Heterogeneous dislocation structures lead to a heterogeneous distribution of stresses as rationalized by the composite model of Mughrabi (1983). In an ordered dislocation structure (as sketched in Figure 7) dense dislocation walls separate adjacent dislocation-depleted regions. When applying an external load, initially all regions deform elastically. With increasing load, the resolved shear stress on individual slip systems reaches the critical resolved shear stress and plastic deformation occurs by motion of dislocations. As regions of high dislocation density exert a higher resistance against plastic deformation than dislocation-depleted regions, the later will yield first. Activation of dislocation glide in dislocation-depleted regions causes dislocations to move towards the dislocation walls. As long as the walls do not yield plastically, these dislocations cannot move further and become trapped at the interface between the walls and the dislocation-depleted regions.

Edge dislocations trapped at an interface between dislocation-depleted regions and dislocation walls cause two different effects (illustrated in Figure 8): 1) their Burgers vector component perpendicular to the boundary plane leads to an orientation difference between both sides, i.e. between the dislocation-depleted region and the dislocation wall, and 2) the component parallel to the wall generates elastic stresses along the direction of the applied load. These elastic stresses increase the applied stress in the wall (forward stresses), but reduce the elastic stresses in the dislocation-depleted regions (back stresses). The forward stresses in the walls increase the resolved shear stresses there and lead eventually to the
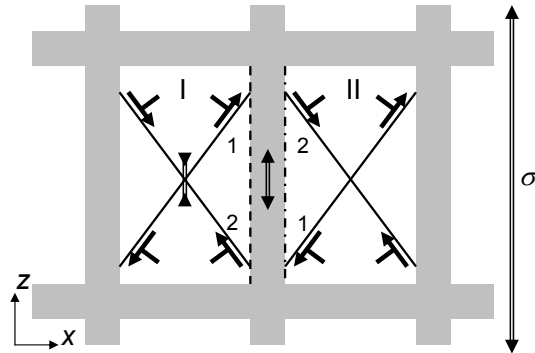
Fig. 7: Sketch of an ordered dislocation structure with dislocation walls (grey) separating dislocation-depleted regions (white). When a tensile load is applied vertically, two slip systems in each of the two dislocation-depleted regions are activated. The Burgers vectors of the edge dislocations creating the plastic deformation are indicated. Dislocations become trapped at the interfaces (dashed or dashed-dotted).

onset of plastic deformation in the walls; then mobile dislocations can penetrate into (and even through) the dislocation walls.

The internal stresses caused by the interface dislocations change the elastic strain state in both regions. Along the tensile direction, the elastic strains are increased in the walls (forward strains) and decreased in the dislocation-depleted regions (back strains) with respect to the tensile elastic strains caused by the applied load. In the directions perpendicular to the tensile direction, (relative) compressive strains in the walls and (relative) tensile strains in the dislocation-depleted regions are developed due to elastic cross contraction.
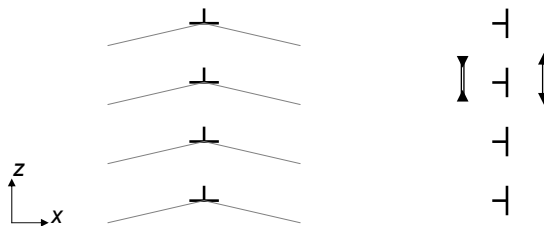


Fig. 8: Sketch of two vertical planar arrangements of edge dislocations trailing along the $y$-direction into the drawing plane: (left) edge dislocations with Burgers vectors perpendicular to the boundary plane form a tilt boundary with an orientation difference on both sides and (right) edge dislocations with Burgers vectors in the boundary plane form an interface with tensile and compressive elastic stresses.

3.2 Asymmetry of radial peak profiles. The presence of heterogeneous elastic strains causes an asymmetry of radial peak profiles, such as in Figure 3 (Ungár et al. 1984; Mughrabi et al. 1986). In terms of the classical composite model, the total radial profile is explained as superposition of two subprofiles (as sketched in Figure 9(left)): one from the dislocation walls broadened by the high dislocation content therein and another from the dislocation-depleted regions being narrower due to their lower (but existing) dislocation content.

For reflections with scattering vector close to the tensile axis, the elastic strain parallel to the tensile axis is probed (axial case). According to Eq. (2) the forward (relative tensile) elastic strains in the walls cause a shift of the wall subprofile towards smaller Bragg angles and the backward (relative compressive) elastic strains in the dislocation-depleted regions cause a shift of this subprofile towards larger Bragg angles. These mutual shifts of the two subprofiles in their radial positions produce an asymmetric profile with a larger tail on the low-angle side, called a positive asymmetry and shown in Fig. 9(left).

The opposite is true for radial diffraction profiles of Bragg reflections perpendicular to the tensile axis (side case). The compressive elastic strains in the walls cause a shift of the wall subprofile towards larger Bragg angles and the tensile elastic strains in the subgrains cause a shift of the subgrain subprofile towards smaller Bragg angles. In this case an asymmetric profile with a larger tail on the high-angle side is produced (i.e. a negative asymmetry).

The classical composite model — despite being successful in explaining asymmetries of radial profiles and flow stresses — has been seriously criticized, by e.g. Argon and Haasen (1993), for the rather large dislocation content postulated for the dislocation-depleted regions in order to explain the observed broadening of their subprofile and the critical resolved shear stress of the dislocation-depleted regions, because such high dislocation densities have never been observed by TEM.

3.3 Revised composite model. The observation of sharp high-intensity peaks on a structure-less cloud of lower intensity and the properties of the high-intensity peaks summarized in section 2.5 endorse their interpretation as stemming from dislocation-free subgrains. This is further substantiated by the absence of high-intensity peaks in Bragg reflections from deformed grains in a non-cellforming aluminium magnesium alloy (Jakobsen, Poulsen, Lienert, Huang, and Pantleon 2007b). Analogously, the broad, structureless cloud is considered as caused by dislocation walls. The high dislocation densities in the walls broaden the radial profiles forming the low-intensity cloud in a reciprocal space map. Further details about dislocation walls cannot be revealed from the structureless cloud, in particular no information on individual dislocation walls can be retrieved.

The occurrence of back strains for the high-intensity peaks and forward strains for the cloud component discussed in section 2.6 is in general agreement with the composite picture of an ordered dislocation structure. The two other findings for the high-intensity peaks, their sharpness and their distribution in radial position, nevertheless, are in conflict with the classical composite model. The observed rather sharp peak profiles indicate their origin from dislocation-free regions with dislocation densities less than $1.2 \cdot 10^{13}$ m$^{-2}$. Therefore, the dislocation-depleted regions are not dislocation cell interiors containing a significant dislocation content as suggested earlier (Ungár et al. 1984; Mughrabi et al. 1986), but almost perfect subgrains with vanishing dislocation density (which also explains, why in the dislocation-depleted regions hardly any dislocations have been found by TEM).

The slightly different radial positions of the high-intensity peaks indicate that each subgrain experiences a slightly different elastic strain. To account for these differences in a composite model, the view on the subprofile originating from the dislocation-depleted regions is revised. Their contribution cannot be described by a shifted profile broadened by dislocations (as the presumed dislocation content is not detected in the subgrains), instead each independently diffracting subgrain contributes with its own particular radial profile. These individual radial profiles are sharp, only affected by instrumental broadening and not broadened by any defect content. They differ in their radial position as each of the dislocation-free regions experiences a slightly different elastic stress (with a back stress in average).

In the revised composite model, the superposition of sharp profiles from all individual subgrains as sketched in Fig. 9(right) replaces the subprofile from cell interiors of the classical composite model. In the sketch, individual radial profiles of only six subgrains are illustrated which are not sufficient to form a smooth and broad contribution. Experimentally, much more distinct subgrains can be identified and analyzed. In this manner, a smooth superposition of the individual profile is achieved.
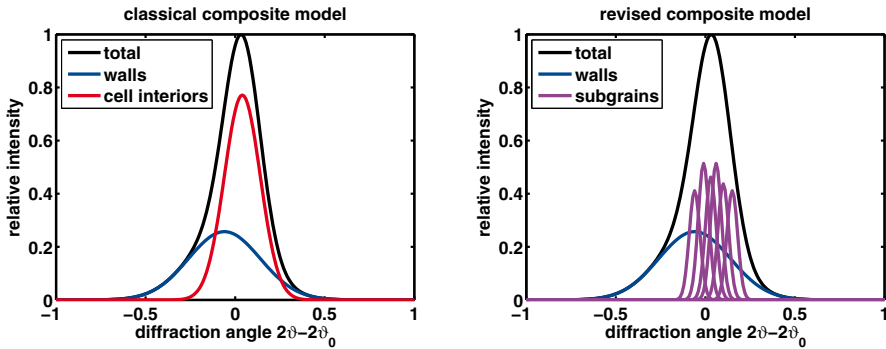


Fig. 9: Decomposition of radial profiles: (left) according to the classical composite model in broadened subprofiles from walls and dislocation-depleted regions (cell interiors) and (right) according to the revised composite model in a broadened profile from the walls and several sharp peaks from individual subgrains.

Presently, the original suggestion that dislocation walls contribute to the radial profile with a subprofile broadened by the high dislocation density in the walls and shifted due to forward stresses has been used unaltered, but, analogously to the individual subgrains, it is reasonable that the subprofile from dislocation walls is a superposition of radial profiles (from individual walls shifted with respect to each other by their individual forward elastic strains) as well. As each profile from a dislocation wall is significantly broadened by the presence of dislocations, the shape of the resulting subprofile from all dislocation walls obtained by superposition is not expected to be much different from the individual profiles. Unfortunately, no information can be gained on individual dislocation walls by reciprocal space mapping with high resolution due to their broadened diffraction profiles and spatial probing is required to differentiate between particular dislocation walls.

3.4 Elastic strains of subgrains. The occurrence of elastic strains in individual subgrains and their differences can be explained on a statistical basis by fluctuations in the active slip systems. A geometrical model taking into account all details of the slip geometry will be presented elsewhere (Jakobsen, Prinz, and Pantleon 2011), here only the main ideas are outlined in connection with Figure 7.

When applying a tensile load along the vertical direction, each of the two adjacent subgrains deforms plastically on two symmetrical slip systems (1 and 2) whereas the connecting dislocation wall deforms only elastically. At the interface, the dislocations get trapped and the total Burgers vector stored at the interface (of height $h$ and shown dashed in Figure 7) with subgrain I evolves according to

$$\dot{B}_x = b_x(\Phi_1 - \Phi_2)h \qquad \text{and} \qquad \dot{B}_z = b_z(\Phi_1 + \Phi_2)h . \qquad (3)$$

The fluxes of dislocations $\Phi_{i,I} = p\dot{\gamma}_i/b$ in both slip systems $i$ are given by the respective strain rates $\dot{\gamma}_i$ and an orientation factor $p$.

The edge dislocations stored at the interface cause (through the $x$-component of their Burgers vectors) an orientation difference between wall and subgrain with an rotation angle $\theta_y = B_x/h$ around the $y$-axis following from the Read–Shockley equation for tilt boundaries (cf. Figure 8(left)); their $z$-component leads analogously to a difference in the elastic strain $\varepsilon_{zz} = B_z/h$ between the wall and the subgrain.

On average, each of the two slip systems is activated equally, but small random fluctuations $\delta\dot{\gamma}_i$ of the strain rate $\dot{\gamma}_i = \dot{\bar{\gamma}} + \delta\dot{\gamma}_i$ around its average value $\dot{\bar{\gamma}}$ may occur. The elastic strain of a particular subgrain evolves accordingly

$$\dot{\varepsilon}_{zz} = -p\frac{b_z}{b}(\dot{\gamma}_1 + \dot{\gamma}_2) = -p\frac{b_z}{b}(2\dot{\bar{\gamma}} + \delta\dot{\gamma}_1 + \delta\dot{\gamma}_2) \tag{4}$$

where the negative sign reflects the formation of backward strains in the subgrain with respect to the adjacent wall deforming only elastically. Consequently, the elastic strains in the subgrains (with respect to the dislocation walls) have a non-vanishing average value

$$\langle\varepsilon_{zz}\rangle = -2p\frac{b_z}{b}\gamma = -\varepsilon_{\mathrm{pl}} \tag{5}$$

exactly opposite to the plastic strain $\varepsilon_{\mathrm{pl}} = 2m\gamma$ in the subgrains (where $m$ is the common Schmid factor of both slip system) as required by compatibility. These considerations are of course only valid as long as the walls stay impenetrable for dislocations and do not deform plastically. When the walls yield plastically, dislocations enter the walls, even pass them or annihilate with other dislocations coming from the wall and the dislocation accumulation at the interface is largely reduced.

The variation of the elastic strains in different subgrains depends only on the nature of the fluctuations. For the case, that fluctuations in the strain rate are caused by variations in the number of mobile dislocations, Pantleon (1997) has shown that the resulting evolving quantities are Gaussian distributed. Fluctuations in the activation of slip systems lead directly to a Gaussian distribution of the elastic strains of the individual subgrains with a standard deviation following from

$$\langle\delta\varepsilon_{zz}^2\rangle = 2p^2\frac{b_z^2}{b^2}\frac{b}{d}\gamma = p\frac{b_z}{b}\frac{b}{d}\varepsilon_{\mathrm{pl}}. \tag{6}$$

Accordingly, the standard deviation of the distribution of elastic strains in the subgrains follows a square root dependence on the plastic strain in the subgrains. For the particular geometry ($p = 1/\sqrt{3}$ and $b_z = 2b/\sqrt{6}$) and the experimental conditions of section 2.5 (a plastic strain of about 2% (neglecting the elastic deformation in the subgrains due to the applied load) and an average subgrain size $d$ of 1.4 $\mu$m) a standard deviation of 0.13% for the elastic strains is predicted, slightly larger than the experimentally observed variation.

The predicted increase in the spread of elastic strains with the square root of the plastic strain in the subgrains according to Eq. (6) cannot continue with increasing strain, because the average elastic energy of subgrains with Gaussian distributed elastic strains is larger than the elastic energy for identical elastic strains in all subgrains (see Jakobsen et al. 2011). Such an enhanced elastic energy and the corresponding elastic stresses will affect the fluctuations in different slip systems in such a manner that the elastic energy and hence the spread in elastic strains is not increasing unlimitedly.

## 4. APPLICATION ON UNIDIRECTIONAL DEFORMATION

4.1 Subgrain dynamics during incremental tensile loading. The evolution of the subgrains is monitored in a bulk grain of another polycystalline copper sample by deforming it from 3% to 4.2% tensile strain in small incremental steps of about 0.04% (Jakobsen et al. 2006). After each strain increment a three-dimensional reciprocal space map of a subvolume of the grain has been gathered while rocking over $0.32°$ in 80 intervals of $0.004°$. Analysis of about 20 high-intensity peaks revealed a rather intermittent dynamics: subgrains appear and disappear during straining, some even exist only for a short strain interval; for example, the high-intensity peak in Figure 10 exists for a strain interval of about 0.2%. New distinct diffraction peaks emerge from the cloud of lower intensity. Correspondingly, new dislocation-free regions materialize in regions formerly occupied by dislocations.
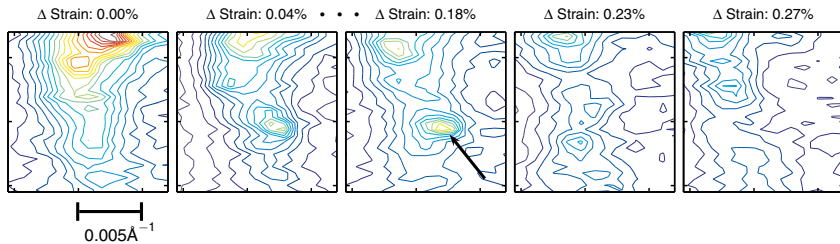


Fig. 10: Example for subgrain dynamics during incremental tensile loading. The subfigures are excerpts from larger projection onto the azimuthal plane and given as function of external strain with strain increments relative to the first map. A high-intensity peak appears, grows in intensity and disappears again. The arrow indicates the peak at its maximum intensity (from Jakobsen et al. 2006).

4.2 Structure formation during continuous tensile loading. After the discovery of ordered dislocation structures in thin foils by TEM, the relation between the observed structures and the dislocation structures present in the specimen before preparation of a thin foil and before unloading after deformation has been debated intensively (see Seeger 1988). Relaxation of the structure due to foil preparation can be avoided by neutron irradiation fixing the formed dislocation structure (Essmann 1963). By irradiating a deformation structure under load, the existence of ordered dislocation structures after terminating the deformation has been proven and observed differences between the dislocation structures in the loaded and unloaded state rationalized (Mughrabi 1971). The lack of *in-situ* investigations, however, has left the question of the existence of ordered dislocation structures during the course of deformation unanswered. This issue cannot be settled by incremental loading steps as ordering may occur in the short relaxation intervals.

To establish the emergence of ordered dislocation structures during deformation a fully dynamic experiment has been conceived where a copper specimen is loaded without interruption for data taking while monitoring a 400 reflection of an individual bulk grain (Pantleon, Wejdemann, Jakobsen, Lienert, and Poulsen 2009). A bulk grain smaller than the beam size is centered in the beam and its corresponding 400 reflection close to the tensile axis centered at the far distant detector. The sample is strained in tension continuously from the undeformed state with a low strain rate of $6 \cdot 10^{-7}$ s$^{-1}$ while obtaining reciprocal space maps by rocking. Each map consists of only 15 rocking intervals of $0.005°$ to enhance time resolution. The center of the covered rocking range is adjusted manually during the experiment to compensate for grain rotation.
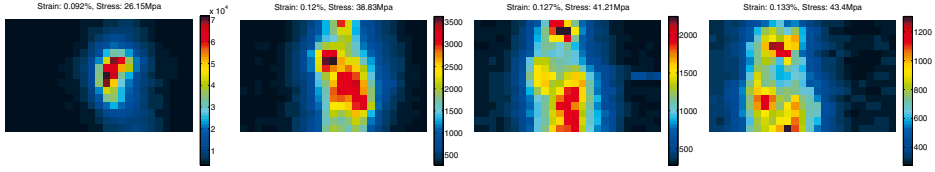
Fig. 11: Projection onto the azimuthal plane of the reciprocal space maps obtained during continuous deformation from undeformed state. The projections are given as function of stress and tensile strain. The images span $25 \cdot 10^{-3}$ Å$^{-1}$ horizontally and $9 \cdot 10^{-3}$ Å$^{-1}$ vertically (rocking direction). Different colour scales are used for different strain levels (from Pantleon et al. 2009).

Projections of the reciprocal space maps onto the azimuthal plane are shown in Figure 11 for four successive strains. Between the first and the second map, re-centering of the grain was required due to grain rotation and during this time no reciprocal space map was obtained. The map of the reflection obtained at 0.09% tensile strain (as all maps at smaller tensile strains) is similar to that of an undeformed grain, with only a slight broadening of the reflection and no clear indication of any grain breakup into different orientations. For the subsequent strain steps (0.120%, 0.127%, and 0.133%), a breakup of the reflection is clearly seen. Several different sharp peaks can be identified in each azimuthal projection indicating the formation of (at least three) different regions of significantly lower dislocation density at this small strain.

The emergence of characteristic features (sharp high-intensity peaks on a cloud of lower intensity) in the Bragg reflection must be attributed to the presence of several dislocation-free regions in the grain during deformation. With this observation, formation and existence of ordered dislocation structures during tensile deformation is proven beyond any doubt.

4.3 Stress relaxation. For assessing the stability of dislocation structures during interrupted tensile tests, the effect of stress relaxation on the dislocation structure has been investigated (Jakobsen, Poulsen, Lienert, Bernier, Gundlach, and Pantleon 2009): Another copper sample is preloaded in small steps to a tensile strain of 1.82%. By following the movement of the grain during this incremental straining, a calibration curve is produced relating the displacement of the tension motor to the macroscopic strain and the spatial grain movement. The sample is then strained continuously with a strain rate of $1.1 \cdot 10^{-6}$ s$^{-1}$ to a tensile strain of 2.315%. During this first slow loading 20 reciprocal space maps are gathered. After that, the tension motor is stopped and the sample held at constant position of the tension motor for 41 hours, during which the tensile strain increases to 2.365%. During the first hour another 19 reciprocal space maps are gathered. After re-centering of the grain with respect to the beam, the sample is strained continuously with the same strain rate of $1.1 \cdot 10^{-6}$ s$^{-1}$ to a tensile strain of 2.682%. During this period 14 reciprocal space maps are gathered. The sample is then held at constant motor position for 2.2 hours, while gathering 10 maps during the first 45 minutes. At the end of the hold, the strain has increased to 2.695%.

Based on the identification of individual peaks with individual subgrains, the time evolution of the intensity distribution can be rationalized in terms of rotation, straining and growth or shrinkage of subgrains. As an example, Figure 12 provides a tableaux of azimuthal projections of the intensity distributions at the end of the second loading stage and during the second hold. During loading stages significant changes in the subgrain structure are observable in the reciprocal space maps. Temporary formation of new subgrains and

disappearance of others can be recognized. During the entire tensile loading subgrains of different orientations and elastic strains appear and disappear intermittently. From visual comparison of the reciprocal space maps obtained during both holding stages, there is no evidence of any microstructural change on the subgrain level within the first hour of data taking after stopping the tension motor (see azimuthal projections of the second holding stage in Figure 12). Extrapolation of the evolution during holding to times prior to the moment of stopping and comparison with the last reciprocal space map during loading even rules out any hypothetical structural changes at the subgrain level, which may occur at the exact time of stopping and is completed before the first measurement during holding.

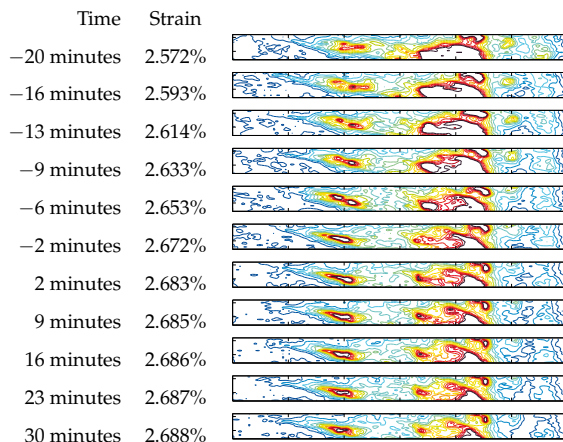| Time | Strain | |
|---|---|---|
| −20 minutes | 2.572% | |
| −16 minutes | 2.593% | |
| −13 minutes | 2.614% | |
| −9 minutes | 2.633% | |
| −6 minutes | 2.653% | |
| −2 minutes | 2.672% | |
| 2 minutes | 2.683% | |
| 9 minutes | 2.685% | |
| 16 minutes | 2.686% | |
| 23 minutes | 2.687% | |
| 30 minutes | 2.688% | |

Fig. 12: Azimuthal projection of the last six reciprocal space maps obtained during the second slow loading and every second of the reciprocal space maps obtained during the second holding. Time is with respect to the moment when the tension motor is stopped, and for the center image of each data set. The projections each cover $[0\text{Å}^{-1}, 0.12\text{Å}^{-1}]$ horizontally and $[0.027\text{Å}^{-1}, 0.036\text{Å}^{-1}]$ vertically. The colours are in arbitrary units of integrated intensity (Pantleon et al. 2009).

Additional insight is gained from integrated radial peak profiles. Two quantities of interest can be derived (e.g. Ungár 2001; Kučel 2007): the average elastic strain (along the diffraction vector) with respect to the initial, unloaded state, and the width of the strain distribution. Both are determined from fitting a pseudo-Voigt function to the radial peak profile as center (identical to the average) and full width at half of the maximum intensity. Both quantities are plotted in Figure 13 as function of time during the loading and holding sequence.

During the loading stages the mean position of the radial profile decreases and hence the average elastic strain in the illuminated grain increases (cf. Eq. (2)) with increasing stress. During the holding period the elastic strains decrease due to stress relaxation. Relaxation of the elastic strain seemingly comprises two components (in particular after the first loading): a fast initial transient, followed by a much slower response. Correspondingly, the width of the internal strain distribution (as observed from the width of the radial profiles) increases during tensile loading, and decreases almost linearly with time during the first hour after stopping the tension motor.

The microstructure (as described in terms of the number of subgrains, their orientation and extension in reciprocal space) develops markedly and in an intermittent manner during continuous loading, but becomes frozen at the instant of interrupting the traction. Within the

observation time, individual dislocations migrate under the applied load further in forward direction. Their motion causes additional plastic deformation of the gauge section of the specimen and hence a specimen elongation. Consequently, the fixed displacement of the motor position requires less elastic deformation and the average elastic strain decreases.
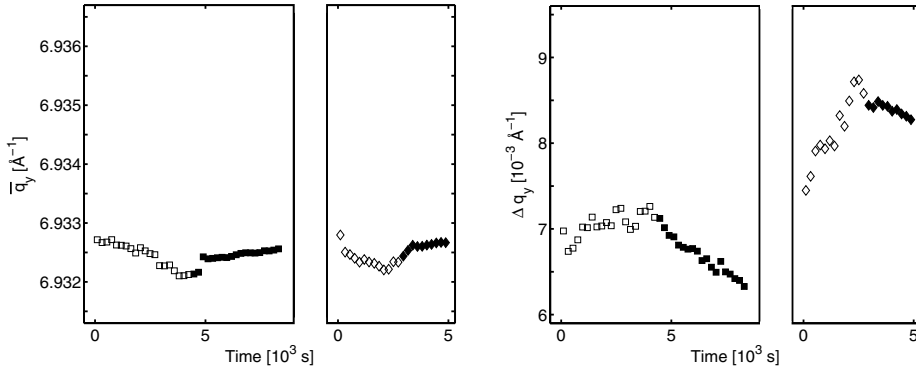


Fig. 13: Average value $\bar{q}_y$ (left) and full width at half of the maximum intensity $\Delta q_y$ (right) of the radial peak profiles as function of time. First slow loading (open square) and holding (filled square), second slow loading (open diamond) and holding (filled diamond). The time in each part is measured with respect to the start of deformation (from Jakobsen et al. 2009).

## 5. APPLICATION ON STRAIN PATH CHANGES

5.1 General. The effect of strain path changes is investigated here for tension-tension sequences where pre-deformation in tension is followed by a second tensile deformation along a different direction (Wejdemann et al. 2009; 2010a). Such simple strain path changes involving only two different straining stages are characterized by the parameter

$$\alpha = \frac{\dot{\varepsilon}_1 : \dot{\varepsilon}_2}{\|\dot{\varepsilon}_1\| \|\dot{\varepsilon}_2\|} \tag{7}$$

where $\dot{\varepsilon}_1$ and $\dot{\varepsilon}_2$ are the strain rate tensors of the first and second stage (Schmitt, Shen, and Raphanel 1994). The effect of strain path changes is largest for $\alpha = 0$, called an orthogonal strain path change. The extreme cases $\alpha = 1$ and $\alpha = -1$ correspond to monotonic deformation and complete strain reversal, respectively. For tension-tension sequences $\alpha$ can take values between $-0.5$ and 1.

To establish the initial deformation prior to any strain path change fully recrystallized copper sheets are pre-deformed in tension to 5% plastic strain with a strain rate of $1.4 \cdot 10^{-4}$ s$^{-1}$, before smaller dog-bone shaped samples are spark cut from the sheets for further tensile deformation. The samples are cut under four different angles $\theta$ (0°, 35°, 55° and 90°) between the pre-deformation tensile axis and the new tensile axis. Assuming volume-conserving plasticity their strain path change parameters are 1, 0.5, 0, and $-0.5$, respectively.

The four samples are mounted in the load frame one at a time. In order to stabilize the samples, they are subjected to a small load corresponding to a plastic strain of 0.2%. For each sample a suitable grain is selected, and a particular 400 reflection close to the tensile

axis is mapped at different strain levels. The samples are deformed in tension (with a strain rate of $1 \cdot 10^{-4}$ s$^{-1}$). At selected strain levels the traction is interrupted and for each sample 11 maps covering the entire orientation spread of the selected grain are obtained between 0.2% and 5%. A typical map covering 3° is comprised of 200 single images recorded while rocking through an interval of 0.015°.

5.2 Data analysis. Before the individual images are combined to three-dimensional reciprocal space maps, they are subjected to three pre-processing steps (Wejdemann et al. 2009). First, the background level around the 400 reflection is estimated for each image and subtracted from the intensity. Second, the intensity in the image is normalized by the beam intensity, which is measured at the beam stop behind the sample during acquisition. Third, cosmic rays are identified in each image by comparing the intensity on a pixel-by-pixel basis with the images taken just before and after. If found, cosmic rays are removed by linear interpolation between those neighboring images.
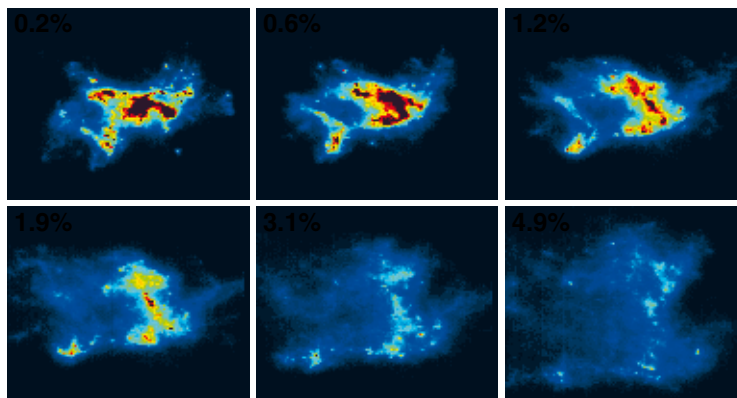


Fig. 14: Azimuthal projection of three-dimensional reciprocal space maps after strain path change by a tension-tension sequence with 90° between the first and second tensile axis. The indicated strains represent the strain along the second tensile axis only (Wejdemann et al. 2009).

Azimuthal projections from 6 different strains (along the second tensile axis) are shown in Figure 14 for the sample with 90° between the tensile axes. The heterogeneous structure of the intensity distribution with high-intensity peaks on a low-intensity spread-out cloud can be seen. The sequence of projections illustrates the advantage of the experimental method for studying the dynamics of deformation structures in an individual grain in reciprocal space *in-situ*. The figure shows that for larger strains the general intensity level decreases as the intensity distribution spreads out, and the peaks become less prominent. The apparent disappearance of the peaks as the strain is increased is partly an effect of the general decline of the intensity level, because the same colour scale is used for all projections. This illustrates the general difficulty to visually assess how much of the intensity distribution has to be classified as peaks because the appearance depends strongly on the colour scale.

5.3 Subgrain volume fraction. An automatic partitioning of the intensity distribution into two components (peaks and cloud) is achieved by a newly developed fitting method (Wejdemann et al. 2009; 2010b) which allows to separate the contribution of peaks caused by diffraction from subgrains from the contribution of the cloud caused by diffraction from dislocation walls and to analyze each part separately.

After partitioning the intensity distributions the subgrain volume fraction is calculated for all reciprocal space maps by dividing the intensity in the peak component with the total intensity in the map. Figure 15(left) shows that the sample with 55° between the tensile axes has the smallest subgrain volume fraction for all strains. The other three samples show approximately the same subgrain volume fraction for strains up to 1.5% after which the sample with 0° shows the largest subgrain volume fraction and the samples with 35° and 90° lie between the extremes. Figure 15(right) shows the results relative to the values at the smallest strain. It shows that the rate of decrease of the subgrain volume fraction is largest for the 55° sample and smallest for the 0° sample, with the other samples in between.

The observed variations in subgrain volume fraction can be rationalized with the help of the strain rate change parameter: The results in Figure 15 show a systematic effect of the degree of strain path change as measured by the strain path change parameter on the subgrain volume fraction. A smaller absolute value of $\alpha$ corresponds to a larger rate of decrease of the subgrain volume fraction. The findings are consistent with TEM observations on copper, which indicate that tension-tension strain path changes lead to an increase in the wall thickness (Schmitt et al. 1991). Such an increase in the wall thickness will lead to a decrease in the subgrain volume fraction as observed here.
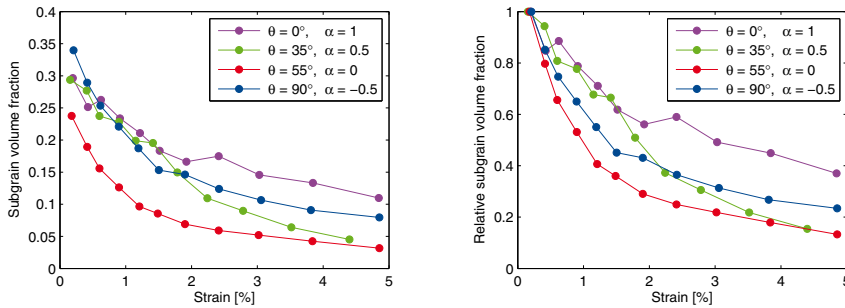


Fig. 15: Subgrain volume fraction during stain path changes as a function of strain for the four different samples: absolute values (left) and relative values (right) (from Wejdemann et al. 2009).

5.4 Asymmetry of radial profiles. In order to investigate the effect of a strain path change on the radial profile asymmetry two additional copper samples are cut from a copper sheet pre-deformed in tension (Wejdemann et al. 2010a). One (the 0° sample) is cut with the new (*in-situ*) tensile axis parallel to the pre-deformation axis, and the other (the 90° sample) is cut with the *in-situ* tensile axis perpendicular to the pre-deformation axis.

The samples are mounted in the load frame one at a time, and a small load corresponding to a strain of ∼0.03% is applied for stabilization purposes. For the 0° sample, the scattering vector, the *in-situ* tensile axis and pre-deformation tensile axis are parallel corresponding to the axial case and a positive peak profile asymmetry is expected throughout the experiment. In contrast to this, for the 90° sample the scattering vector and the *in-situ* tensile axis (which are parallel) are perpendicular to the pre-deformation tensile axis. For each sample four suitable grains are selected. For each of the selected grains a reciprocal space map of one particular 400 reflection is obtained and the sample is deformed in unidirectional tension with a strain rate of ∼$10^{-4}$ s$^{-1}$. At 7 different strain levels (up to a tensile strain of 1%) the deformation is paused (allowing the load to relax slightly) while additional reciprocal space maps of the same 400 reflections are obtained.
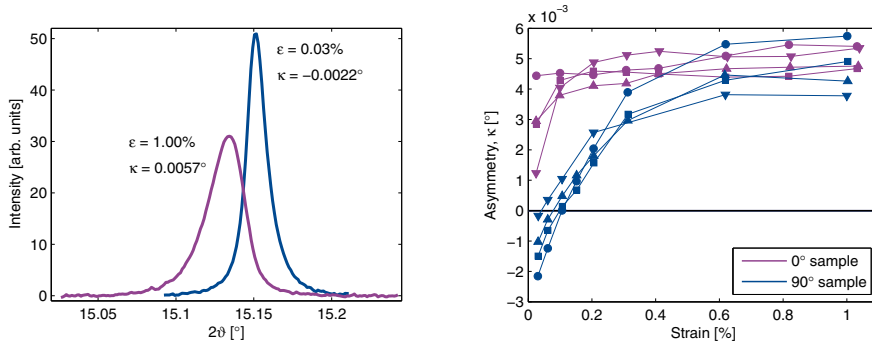
Fig. 16: (left) Radial peak profiles from the same grain from the 90° sample. The strain $\varepsilon$ along the *in-situ* tensile axis and the asymmetry $\kappa$ is indicated. The profiles are normalized to have an area of one. (right) Peak profile asymmetry $\kappa = 2\vartheta_{\max} - 2\vartheta_{\mean}$ (from Wejdemann et al. 2010a).

Radial profiles are calculated from the reciprocal space maps in a $2\vartheta$-range centered on the position of maximum intensity and with a width of 8 times the full width at half maximum intensity. Two examples of peak profiles from the same grain from the 90° sample are shown in Figure 16. The profiles shown are measured at the first and last strain value. As the sample is deformed, the profiles shift to lower values of $2\vartheta$ (due to the average elastic strain caused by the imposed external load), widen (due to dislocation accumulation and heterogeneous elastic strains) and change asymmetry (from having the slower-decaying tail on the high-$2\vartheta$ side to having it on the low-$2\vartheta$ side of the intensity maximum).

The shift in asymmetry can be quantified by the parameter $\kappa = 2\vartheta_{\max} - 2\vartheta_{\mean}$, where $\vartheta_{\max}$ and $\vartheta_{\mean}$ are the Bragg angles of the maximum and the mean of the profile, respectively. Assuming that $\vartheta_{\max}$ coincides with the maximum of the subgrain subprofile (see Hecker, Thiele, and Holste (1998) for theoretical arguments and Jakobsen et al. (2007a) for experimental confirmation), $\kappa$ will be equal to twice $\Delta\vartheta$ for the subgrains and from Eq. (2) it follows that $\kappa$ is proportional to the mean elastic strain in the subgrains. $\vartheta_{\mean}$ can be easily calculated from the profile, but to get a measure for $\vartheta_{\max}$ with sub-pixel accuracy a split pseudo-Voigt function is fitted to each profile. In this way the peak profile asymmetry is determined for the 8 different grains as a function of strain along the *in-situ* tensile axis and shown in the right part of Figure 16. The figure shows that the curves generally fall in two groups. The grains from the 0° sample show a more or less constant peak profile asymmetry while the grains from the 90° sample start with a negative peak profile asymmetry which becomes positive and reaches the level of the 0° sample grains with increasing deformation.

The results in Figure 16 can be understood in terms of the classical composite model. As described above, in deformed metals with a dislocation structure consisting of walls and subgrains, the composite model predicts that peak profiles may be asymmetric because the intragrain stresses shift the wall and subgrain subprofiles with respect to each other. For the 0° sample (for which the *in-situ* and pre-deformation tensile axes are parallel) the intragrain stresses that have developed during pre-deformation do not change significantly during the following *in-situ* deformation and a positive asymmetry is observed for all strains. For the 90° sample (for which the *in-situ* and pre-deformation tensile axes are perpendicular) the intragrain stresses developed during pre-deformation give rise to a negative asymmetry before the *in-situ* deformation. As the sample is deformed along the *in-situ* tensile axis, the intragrain stresses gradually change leading to a positive asymmetry at the same level as for

the 0° sample. The initial negative asymmetry for the 90° sample is caused by the Poisson effect and the strains involved in this will be only a fraction (given by the Poisson ratio) of the strains in the direction of the pre-deformation and have the opposite sign. The Poisson ratio for polycrystalline copper, 0.34, fits well with the asymmetries measured before the *in-situ* deformation: For the 90° sample the values of $\kappa$ are roughly one third the size of the asymmetries for the 0° sample, and have the opposite sign.

## 6. CONCLUSION

With high angular resolution three-dimensional X-ray diffraction quantitative information is gained about dislocation structures in individual bulk grains in macroscopic specimens under various deformation conditions:

1. In three-dimensional reciprocal space maps of tensile deformed copper, individual almost dislocation-free subgrains are identified as high-intensity peaks whereas dislocation walls manifest themselves as a smooth cloud of lower intensity.

2. The elastic strains show only small variations within each subgrains, but larger variations between different subgrains. In average, subgrains experience back strains (with respect to the average elastic strain of the grain) and their radial positions are gathered around the peak of the radial profile, whereas dislocations walls are under forward strains.

3. Intermittent subgrain dynamics is discovered tracing individual subgrains during incremental loading.

4. In uninterrupted tensile test, individual high-intensity peaks in the reciprocal space maps are observed already at about 0.1% strain. The emergence of the characteristic feature of dislocation-free regions proofs that ordered dislocation structures form during tensile deformation and are not caused by any relaxation phenomenon.

5. When tensile loading is terminated, the deformation structure freezes, and a clean-up process gives rise to stress relaxation.

6. After changes of the tensile direction, the volume fraction of the subgrains decreases with strain showing a systematic correlation with the degree of the strain path change.

7. After an orthogonal change in tensile direction, a reversal of the symmetry of radial profiles is observed which is rationalized in terms of the composite model.

In summary, high resolution reciprocal space mapping offers a versatile tool to trace changes in dislocation structures *in-situ* during different loading conditions.

## ACKNOWLEDGEMENT

## REFERENCES

Argon, A.S., and Haasen, P. (1993). A new mechanism of work hardening in the late stages of large strain plastic flow in fcc and diamond cubic crystals. Acta metall. mater. 41, 3289-3306.

Breuer, D., Klimanek, P., and Pantleon, W. (2000). X-ray determination of dislocation density and arrangement in plastically deformed copper. J. Appl. Cryst. 33, 1284-1294.

Essman, U. (1963). Die Versetzungsanordnung in plastisch verformten Kupfereinkristallen. phys. stat. sol. 3, 932-949.

Gil Sevillano, J. (1993). Flow stress and work hardening. In: Mughrabi, H. (ed.). Plastic deformation and fracture of materials, Cahn, R.W., Haasen, P., and Kramer, E.J. (eds.). Materials science and technology, Vol. 6 (VCH, Weinheim, Germany), p. 19-88.

Göttler, E. (1973). Versetzungsstruktur und Verfestigung von [100]-Kupfereinkristallen. I. Versetzungsanordnung und Zellstruktur zugverformter Kristalle. Philos. Mag. 28, 1057-1076.

Hecker, M., Thiele, E., and Holste, C. (1998). Influence of heterogeneous dislocation arrangements on X-ray diffraction profiles measured on cyclically deformed nickel single crystals. Z. Metallkd. 89, 203-210.

Huang, X. (1998). Grain orientation effect on microstructure in tensile strained copper. Scripta mater. 38, 1697-1703.

Jakobsen, B., Poulsen, H.F., Lienert, U., Almer, J., Shastri, S.D., Sørensen, H.O., Gundlach, C., and Pantleon, W. (2006). Formation and subdivision of deformation structures during plastic deformation. Science 312, 889-892.

Jakobsen, B., Poulsen, H.F., Lienert, U., and Pantleon, W. (2007a). Direct determination of elastic strains and dislocation densities in individual subgrains in deformation structures. Acta mater. 55, 3421-3430.

Jakobsen, B., Poulsen, H.F., Lienert, U., Huang, X., and Pantleon, W. (2007b). Investigation of the deformation structure in an aluminium magnesium alloy by high angular resolution three-dimensional X-ray diffraction. Scripta mater. 56, 769-772.

Jakobsen, B., Lienert, U., Almer, J., Poulsen, H.F., and Pantleon, W. (2008). Direct determination of strains in bulk subgrains and dislocation walls by high angular resolution three-dimensional X-ray diffraction. Mater. Sci. Eng. A 483-484, 641-643.

Jakobsen, B., Poulsen, H.F., Lienert, U., Bernier, J., Gundlach, C., and Pantleon, W. (2009). Stability of dislocation structures in copper towards stress relaxation investigated by high angular resolution 3D X-ray diffraction. phys. stat. sol. (a) 206, 21-30

Jakobsen, B., Prinz, M., and Pantleon, W. (2011). Distribution of elastic strains of individual subgrains after tensile deformation. Acta mater. (in preparation).

Knoesen, D., and Kritzinger, S. (1982). Dislocation cell boundary widths and dislocation cell sizes in deformed copper. Acta metall. 30, 1219-1222.

Krivoglaz, M.A. (1996). X-ray and neutron diffraction in non-ideal crystals (Springer, Berlin, Germany) 466 p.

Kužel, R. (2007). Kinematical diffraction by distorted crystals - dislocation X-ray line broadening. Z. Kristall. 222, 136-142.

Larson, B.C., Yang, W., Ice, G.E., Budai, J.D., and Tischler, J.Z. (2002). Three-dimensional X-ray structural microscopy with submicrometer resolution. Nature 415, 887-890.

Mughrabi, H. (1971). Elektronenmikroskopische Untersuchung der Versetzungsanordnung verformter Kupfereinkristalle im belasteten Zustand. I. Die Versetzungsanordnung am Ende von Bereich I. Philos. Mag. 23, 869-895.

Mughrabi, H. (1983). Dislocation wall and cell structures and long-range internal stresses in deformed metal crystals. Acta mater. 31, 1367-1379.

Mughrabi, H., Ungár, T., Kienle, W., and Wilkens, M. (1986). Long range internal stresses and asymmetric X-ray line broadening in tensile deformed [100]-oriented copper single crystals. Philos. Mag. A 53, 793-813.

Pantleon, W. (1997). On the statistical origin of disorientations in dislocation structures. Acta mater. 46, 451-456.

Pantleon, W., Wejdemann, C., Jakobsen, B., Lienert, U., and Poulsen, H.F. (2009). Evolution of deformation structures under varying loading conditions followed in-situ by high angular resolution 3DXRD. Mater. Sci. Eng. A 524, 55-63.

Poulsen, H.F., Nielsen, S.F., Lauridsen, E.M., Schmidt, S., Suter, R.M., Lienert, U., Margulies, L., Lorentzen, T., and Juul Jensen, D. (2001). Three-dimensional maps of grain boundaries and the stress state of individual grains in polycrystals and powders. J. Appl. Cryst. 24, 751-756.

Raj, S.V., and Pharr, G.M. (1986). A compilation and analysis of data for stress dependence of the subgrain size. Mater. Sci. Eng. 81, 217-237.

Sakharova, N.A., and Fernandes, J.V. (2006). Dislocation Microstructure in Copper Multicrystals Deformed under the Sequences: Rolling - Tension and Tension - Rolling. Mater. Sci. Forum 514-516, 589-593.

Seeger, A. (1988). Thermodynamics of Open Systems, Self-Organization and Crystal Plasticity. In: Kettunen, P.O., et al. (Eds.). Proc. 8th Intern. Conf. on Strength of Metals and Alloys, Tampere, Finland (Pergammon Press, Oxford, United Kingdom), p. 463-468.

Schmitt, J.H., Fernandes, J.V., Gracio, J.J., and Vieira, M.F. (1991). Plastic behaviour of copper sheets during sequential tension tests. Mater. Sci. Eng. A 147, 143-154.

Schmitt, J.H., Shen, E.L., and Raphanel, J.L. (1994). A parameter for measuring the magnitude of a change of strain path: Validation and comparison with experiments on low carbon steel. Int. J. Plast. 10, 535-551.

Steeds, J.W. (1966). Dislocation arrangement in copper single crystals as a function of strain. Proc. Roy. Soc. A 292, 343-373.

Ungár, T. (2001). Dislocation densities, arrangements and character from X-ray diffraction experiments. Mater. Sci. Eng. A 309-310, 14-22.

Ungár, T., Mughrabi, H., Rönnpagel, D., and Wilkens, M. (1984). X-ray line broadening study of the dislocation cell structure in deformed [001]-oriented copper single crystals. Acta metall. 32, 333-342.

Wejdemann, C., Poulsen, H.F., Lienert, U., and Pantleon, W. (2009). The effect of strain path change on subgrain volume fraction determined from in situ X-ray measurements. IOP Conf. Ser.: Mater. Sci. Eng. 3, 012003, 6pp.

Wejdemann, C., Lienert, U., and Pantleon, W. (2010a). Reversal of asymmetry of X-ray peak profiles from individual grains during a strain path change. Scripta mater. 62, 794-797.

Wejdemann, C., Lienert, U., Nielsen, H.B., and Pantleon, W. (2010b). Identifying individual subgrains in evolving deformation structures by high angular resolution X-ray diffraction. In: Proc. 31st Intern. Risoe Symp. on Materials Science (Risø DTU, Roskilde, Denmark), 11 pp.

Wilkens, M. (1970a). The determination of density and distribution of dislocations in deformed single crystals from broadened X-ray diffraction profiles. phys. stat. sol. (a) 2, 359-370.

Wilkens, M. (1970b). Theoretical aspects of kinematical X-ray diffraction profiles from crystals containing dislocation distributions. In: Simmons, J.A., de Wit, R., Bullough, R, (eds.). Fundamental aspects of dislocation theory, Vol. II (Nat. Bur. Stand. (US) Spec. Publ. No. 317, Washington, DC, USA), p. 1195-1221.